Journal of Materials Chemistry A

ROYAL SOCIETY OF CHEMISTRY

PAPER

View Article Online
View Journal | View Issue

Cite this: J. Mater. Chem. A, 2025, 13, 28243

Formation and exploration of polymorphism in WO_3 nanostructures for improved catalytic and chemical sensing performance†

Hakimeh Pakdel,‡[a] Vardan Galstyan, ‡*[ab] Viacheslav Golovanov, [cd] Annalisa D'Arco, [e] Tiziana Mancini,[e] Francesco Mura,[f] Marco Rossi, [f] Stefano Lupi,[e] Alessio Mezzi,[g] Saulius Kaciulis [g] and Elisabetta Comini [a]

Nowadays, the development of functional sensing materials to detect gaseous and volatile organic compounds is of great importance for health and the environment. Doping and functionalization of semiconductor materials, as well as the synthesis of composites, are the most considered methods to improve their sensing performance. In this respect, polymorphic transitions in semiconductor metal oxides and subsequent structural changes offer alternative and efficient strategies to tune the kinetics of redox reactions at their surface. Thus, the polymorphism in transition oxide nanostructures can lead to a significant improvement in their catalytic properties. Here, monoclinic/orthorhombic polymorphic WO_3 nanomaterials are synthesized by the precipitation method. Experimental studies and theoretical modeling of the prepared structures are carried out. The results indicate that the composition of the solvent is a crucial factor in the formation and shape of WO_3 nanoparticles. The use of polyethylene glycol as a surfactant increases the degree of structural disorder, suppresses the formation of hydrates, and affects the oxygen content in WO_3. These effects, in combination with the formation of monoclinic/orthorhombic n–n junctions in the WO_3 polymorph, dramatically increase its sensitivity to acetone molecules. In particular, the response of the synthesized WO_3 polymorph is up to 8 times greater compared to the single-phase monoclinic structure. Hence, appropriate modification of the WO_3 crystal structure and formation of monoclinic/orthorhombic junctions in the nanomaterial can significantly improve its sensing performance to acetone without using dopants, mixture materials, or catalytic layers. The performed experimental studies and theoretical modeling to describe the influence of monoclinic/orthorhombic polymorphism on the sensing performance of WO_3 are important and may provide new insights into its applications in monitoring systems and heterogeneous catalysis.

Received 2nd June 2025
Accepted 24th July 2025

DOI: 10.1039/d5ta04439a

rsc.li/materials-a

1. Introduction

Semiconductor nanomaterials, with their large surface area and tunable electronic properties, are among the most studied structures for the development of heterogeneous catalytic systems. These materials generally exhibit promising properties leading to their application in chemical gas sensing, light harvesting, energy storage and conversion.[1–5] Health and safety issues related to air pollution and the ever-growing industrial activities are increasing the need for chemical gas sensors based on semiconductor materials widely used for air quality monitoring and medical diagnosis.[6–9] The adsorption and desorption reactions of oxidizing and reducing gaseous compounds on the surface of semiconductor nanostructures lead to a change in their electrical conductivity. This characteristic feature enables the fabrication of small-size and easy-to-use sensing devices.[10–12] Various approaches, such as functionalization by catalytic layers and the synthesis of composite structures, have been proposed to improve the redox reactions at the surface of semiconductors.[13–16] Furthermore, the synthesis of heterojunctions with improved charge separation and transport properties dramatically impacts the catalytic activity of gas sensors.[2,8,17–20] In this context, polymorphism in

[a]Sensor Lab, Department of Information Engineering, University of Brescia, Via Valotti 9, 25133 Brescia, Italy. E-mail: vardan.galstyan@cnr.it
[b]Institute of Materials for Electronics and Magnetism, National Research Council (CNR-IMEM), Parco Area delle Scienze 37/A, 43124 Parma, Italy
[c]Department of Physics, South-Ukrainian University, Staroportofrankovskaya str. 26, 65020, Odessa, Ukraine
[d]Chemistry and Advanced Materials Group, Faculty of Engineering and Natural Sciences, Tampere University, Korkeakoulunkatu 8, P.O. Box 541, Tampere, FI-33014, Finland
[e]Physics Department, University of Rome 'La Sapienza', P.le A. Moro 5, 00185 Rome, Italy
[f]Department of Basic and Applied Sciences for Engineering (SBAI), University of Rome 'La Sapienza', Via Antonio Scarpa 14, Rome, 00161, Italy
[g]ISMN-CNR, PO Box 10, 00015 Monterotondo Stazione, Rome, Italy

† Electronic supplementary information (ESI) available. See DOI: https://doi.org/10.1039/d5ta04439a

‡ These authors contributed equally.

semiconductors is of great interest, and it is currently considered one of the most effective strategies for developing heterogeneous catalytic systems. The formation of phase junctions in polymorphic materials can lead to an improvement in their physicochemical properties.[21–23] Recently, it has been demonstrated that differences in band energy between phases stimulate the separation of photogenerated charge carriers in the oxide material and significantly enhance its photocatalytic activity. Here, the polymorphic phase transformation in TiO_2 and the formation of the anatase-rutile phase junction affected the concentration of surface vacancies, changed the bandgap, and enhanced the separation and mobility of the charge carriers.[22] This led to a drastic increase in the photocurrent of TiO_2 and to the improvement of its photocatalytic activity for converting CO_2 to CO without adding impurities to the material. Thus, the proper formation of different crystalline phases in the same material makes it possible to avoid the introduction of additives and expensive catalytic materials to improve the electronic properties and reactivity.

WO_3 is a versatile material used in sensors and photocatalytic devices.[24–27] It can be crystallized in different phases, such as triclinic, monoclinic, orthorhombic, hexagonal, and tetragonal, depending on the synthesis and annealing conditions.[28,29] The experimental and theoretical findings show that the tunable crystalline structure of the material is a crucial factor for its catalytic applications.[27,30,31] Therefore, WO_3 with different crystalline phases is widely used in the oxidation and decomposition of gaseous compounds.[32,33] Research studies on the addition of suitable elements to the structure of WO_3 nanomaterials to improve their functionality have already achieved considerable success.[25,34,35] Furthermore, coupling WO_3 with other materials and forming heterostructures with efficient charge separation leads to improved catalytic properties of the composite.[36–39]

Recent studies suggest that deeper insights into the structural polymorphism of transition metal oxide nanomaterials offer new opportunities to tune their electronic band structure and the kinetics of redox reactions at their surface.[22,40] Thus, the preparation of polymorphs could be an alternative to optimize the gas sensing response of pure WO_3. Theoretical and experimental studies show that the monoclinic WO_3, with its acidity, is favorable for the interaction with acetone molecules and their decomposition.[41–44] However, the activation energy for the chemisorption of acetone on the material and its decomposition is very high. Therefore, the optimum operating temperature of gas sensors based on pure WO_3 is around 400 °C.[42,45–47] Furthermore, a transition from monoclinic to orthorhombic phases in WO_3 is possible at these temperatures.[28] Although there is a great interest in WO_3 nanostructures, the chemical gas sensing properties of the monoclinic/orthorhombic WO_3, considering the role of phase transition, are not yet known. Therefore, the challenges of gas sensing response of the WO_3 polymorph still need to be addressed.

The use of surfactants for synthesizing WO_3 nanomaterials can play a crucial role in their crystalline properties.[48,49] Such studies can make an important contribution to the development of structures with enhanced sensitivity based on the use of WO_3 polymorphism.

The aim of this work is to synthesize and investigate the gas sensing characteristics of monoclinic/orthorhombic polymorphic WO_3 nanomaterials. Thus, we evaluate the properties of monoclinic/orthorhombic junctions in WO_3 polymorph for application in chemical gas sensing. The structures were prepared by the precipitation method. The influence of synthesis parameters on the formation and shape of the material was analyzed. The gas sensing performance of monoclinic/orthorhombic WO_3 polymorph nanostructure has been comprehensively discussed considering its compositional, morphological, and structural properties. For the first time, the influence of oxygen and hydrate content, as well as the formation of monoclinic/orthorhombic n–n junctions on the charge transfer and chemical sensing characteristics of the material, is discussed in detail based on experimental studies and theoretical modeling. The obtained results are an important contribution to the development of chemical gas sensing materials with high sensitivity and selectivity, as well as to the production of highly efficient catalytic systems.

2. Experimental

2.1 Synthesis of materials

Tungsten(VI) chloride (CAS number: 13283-01-7, Sigma-Aldrich), benzyl alcohol (CAS number: 100-51-6, Sigma-Aldrich), and polyethylene glycol 200 (CAS number: 25322-68-3, Sigma-Aldrich) were used as reagents for the synthesis of the materials. Two solutions were used for preparing WO_3 nanostructures: (i) 1 g of tungsten(VI) chloride (WCl_6) was dissolved in 50 ml of benzyl alcohol and stirred at room temperature for 30 minutes. (ii) The second solution was prepared similarly to the first. However, in this case, 0.2 g of polyethylene glycol 200 (PEG) was added dropwise to the prepared WCl_6 solution. Then both solutions were heated at 80 °C for 13 hours. Subsequently, the resulting powders were washed with ethanol (CAS number: 64-17-5, Sigma-Aldrich) by centrifugation and dried at room temperature. Finally, the precipitates were calcined at 450 °C for 2 hours. In this work, the powder prepared in benzyl alcohol solution with WCl_6 is referred to as WO_3_P_1, and the one synthesized in benzyl alcohol solution with WCl_6 and PEG 200 is referred to as WO_3_P_2.

2.2 Characterization

The crystalline structure of the fabricated materials was investigated using X-ray diffraction spectroscopy (XRD), electron diffraction, and Raman spectroscopy. The Raman spectra were recorded with a Jasco NRS-5100 confocal Raman microscope equipped with a diode laser at 785 nm and a grating of 600 l mm^{-1}, operating at a nominal power of 20 mW. An MPLFLN 100× objective focuses the laser beam onto the sample with a 1

μm spot. The backscattered signal is collected with a cooled (−69 °C) CCD camera. The measurements were carried out in the range of 159–1890 nm with an effective power of 6.0 mW (accumulations: 50, exposure value: 7 s, resolution: 3 cm^{-1}). We performed four spectral measurements for each material and the spectra were processed (baseline correction and data smoothing) using the Spectra Manager™ operating system connected to the Jasco Raman instrument. The second derivative was calculated to detect the spectrum maxima positions.

Attenuated total reflectance (ATR) Fourier-transform infrared (IR) spectra were performed using a FTIR Vertex70 interferometer (Bruker Optics, Ettlingen, Germany) equipped with a thermal source (Globar), an ATR crystal module with a single reflection diamond crystal at 45°, and an RT-DLaTGS wide range detector. The measurements were carried out under vacuum conditions. The IR spectra of WO_3 nanomaterials were acquired at an acquisition rate of 7 kHz in the spectral region of 50–6000 cm^{-1}, averaging 128 scans collected at a spectral resolution of 4 cm^{-1}. Second-derivative analysis was performed by applying a 9-point smoothing filter.[50] ATR-IR data pre- and postprocessing were performed using OPUS™ 8.2.

The morphological analysis of the materials was carried out by a field-emission scanning electron microscope (FESEM, MIRA3 FEG-SEM, TESCAN) and a transmission electron microscope (TEM, F-200, JEOL) equipped with a GATAN RIO16 CMOS camera and an energy dispersive X-ray (EDX) spectrometer for elemental analysis.

X-ray (XPS) and ultraviolet (UPS) photoemission spectra were acquired by using an Escalab 250Xi spectrometer (Thermo Fisher Scientific Ltd, East Grinstead, UK) with a monochromatic Al Kα (1486.6 eV) excitation source. The measurements were performed in an ultra-high vacuum at a base pressure of about 1×10^{-9} mbar, which increased to 1×10^{-8} during the UPS measurements. The spectra were collected at pass energies of 40 and 5 eV for XPS and UPS, respectively, in the standard mode of the electromagnetic lens system, corresponding to an analysis area of approximately 1 mm in diameter. The binding energy (BE) scale was corrected for a low sample charging by positioning the main C 1s peak of aliphatic carbon at BE = 285.0 eV and verifying that the Fermi level corresponds to BE = 0 eV. The work function of the samples was calculated from the cutoff energy at zero intensity in the valence band spectra acquired by using He I source. A series of negative bias voltages in the range of 2–20 V was applied to shift these spectra from the spectrometer threshold. Spectroscopic data were processed by Avantage v.5 software (Thermo Fisher Scientific Ltd).

To perform gas sensing studies, the materials were deposited on alumina substrates (dimensions: 2 mm × 2 mm × 0.75 mm, Kyocera, Japan) using the drop-casting method. Initially, platinum (Pt) interdigitated electrical contacts and a Pt heater were deposited on the surface and the rear side of the substrates using DC magnetron sputtering. Next, the synthesized powdered materials were dispersed in distilled water (H_2O) and

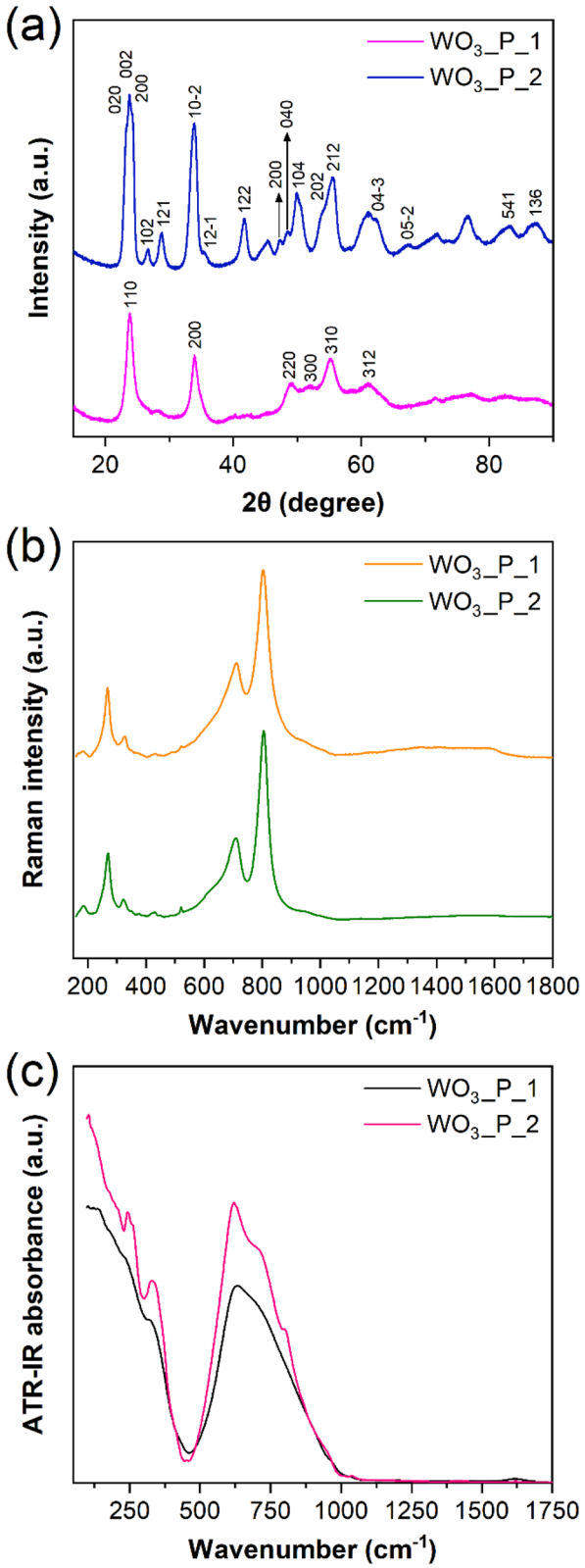

Fig. 1 (a) XRD patterns of WO_3_P_1 and WO_3_P_2 samples. (b) Raman spectra of WO_3_P_1 and WO_3_P_2. (c) ATR-IR spectra of WO_3_P_1 and WO_3_P_2.

drop-cast on the alumina substrates. A Gilson dispenser was used for drop casting. Gas sensing analyses were conducted using the flow-through technique in a thermostatic test chamber, where the humidity level was regulated with a humidity sensor.[51,52] The gas flow rate was 0.3 l min^{-1}. The concentration of each analyte was obtained by mixing the synthetic air with the gas. The sensing response of fabricated structures to reducing gases was calculated according to the following equation:

$$S = \frac{(G_f - G_0)}{G_0} = \frac{\Delta G}{G_0}$$

herein, G_0 is the conductance of material in air and G_f is the steady-state conductance value of the structure in the presence of gas. The response to oxidizing gases was defined as the relative variation of the electrical resistance of sensors (R_0: the resistance of the sensor in air, R_f: the steady-state resistance in the presence of an analyte):

$$S = \frac{(R_f - R_0)}{R_0} = \frac{\Delta R}{R_0}$$

2.3 DFT calculations

Theoretical modeling of the band structure was performed based on the *ab initio*-density functional calculations[53] with plane wave basis and norm-conserving pseudopotentials (CASTEP code).[54] The hybrid PBE0 exchange-correlation functional[55] was used, and the plane wave basis set was limited to a cut-off energy of 800 eV. To sample the Brillouin zone for the W_4O_{12} unit cell, a Monkhorst–Pack grid 2 × 2 × 2 was applied,[56] resulting in two irreducible *k*-points.

3. Results and discussion

3.1 Structural and morphological analysis

Fig. 1(a) shows the XRD patterns of WO_3_P_1 and WO_3_P_2 materials. The XRD pattern of WO_3_P_1 reveals the following main diffraction peaks at 24.1°, 33.96°, 49.36°, 51.96°, 55.13°, and 61.27°, which can be assigned to the (110), (200), (220), (300), (310), and (312) planes of monoclinic phase (JCPDS no. 98-003-9121, space group: *P*1*c*1 and space group number: 7), respectively. In the XRD pattern of WO_3_P_2, the peaks at 23.228°, 23.801°, 24.495°, 26.777°, 28.858°, 50.006°, 80.297°, 87.111° are indexed as (020), (002), (200), (102), (121), (104), (541), (136) planes of orthorhombic phase (JCPDS no. 98-004-9836, space group: *Pbcn* and space group number: 60). The ones at 33.951°, 35.651°, 41.802°, 47.404°, 48.430°, 54.035°, 55.509°, 62.474°, and 67.365° correspond to the (10−2), (12−1), (122), (200), (040), (202), (212), (04−3), and (05−2) planes of monoclinic phase (JCPDS no. 98-007-1692, space group: $P12_1/c1$ and space group number: 14), respectively. The peak intensities of WO_3_P_2 are sharper and narrower than those of WO_3_P_1, which indicates that PEG 200 enhances the crystallinity of WO_3 nanomaterial. Hence, the application of PEG in the synthesis procedure affects the formation of crystalline WO_3 nanostructure.[48,57,58]

Table 1 Raman peak positions and chemical group assignment of WO_3_P_1 and WO_3_P_2 nanomaterials

Frequency position (cm^{-1}) Sample WO_3_P_1	Frequency position (cm^{-1}) Sample WO_3_P_2	Assignment	References
184	186	ν(W–O–W)	62 and 64
		Lattice mode	59
268	270	δ(O–W–O)	59, 62 and 64
328	324	O–W–O deformation mode	62, 64 and 66
		ν(W–OH_2)	59
	353		
370			
	376	Orthorhombic	64
	397		
430	431		59
522	521	Si–O	
	616		
	633	Orthorhombic	64
713	713	ν(O–W–O)	42 and 64
		Monoclinic	59
804	806	Stretching (O–W–O)	59 and 64
940	940	Stretching (W=O)	63 and 64

Raman spectra of WO_3_P_1 and WO_3_P_2 are shown in Fig. 1(b). They both exhibit main vibrational bands at 184, 324, 710, and 805 cm^{-1}, which are generally assigned to the monoclinic phase. The bands located at around 805 and 710 cm^{-1} can be ascribed to the stretching vibration of O–W–O,[59–63] while the one at 324 cm^{-1} corresponds to the O–W–O bending vibration. The peak at 184 cm^{-1} is attributed to the lattice mode, and it is possible to observe a shift to higher frequencies for the WO_3_P_2 sample. Furthermore, unlike the WO_3_P_1 material, peaks and shoulders corresponding to the orthorhombic phase are identified in the spectrum of WO_3_P_2 (Table 1). Here, three main vibrational bands are observed at 269, 376, and 632 cm^{-1}. The bands at 632 and 376 cm^{-1} can be assigned to the stretching vibration of the bridging oxygen O–W–O,[64] while the peak at 269 cm^{-1} is associated with W–O–W deformation.[59,64] The highest frequency peak at 940 cm^{-1} present in both samples, can be attributed the W=O stretching vibration of the terminal oxygen,[63,65] which is usually not present in three-dimensional structures, such as orthorhombic and monoclinic.[64]

The ATR-IR spectra of WO_3_P_1 and WO_3_P_2 are reported in Fig. 1(c), while the absorption frequencies are listed in Table 2 with assignment to the corresponding vibrational modes. The spectrum of the sample WO_3_P_1 recorded in the far-IR region shows main characteristic bands at 348 cm^{-1},

Table 2 Positions of IR absorption peaks and their assignment to vibrational modes of functional groups in WO_3_P_1 and WO_3_P_2 nanomaterials

Frequency position (cm^{-1}) Sample WO_3_P_1	Frequency position (cm^{-1}) Sample WO_3_P_2	Assignment
57	59	Lattice modes
72	75	Lattice modes
87	—	Lattice modes
—	92	Lattice modes
105	105	Lattice modes
120	120	Lattice modes
139	137	Lattice modes
145	148	Lattice modes
—	178	Lattice modes
182	—	Lattice modes
194	194	Lattice modes
—	212	Lattice modes
234	—	ν(W–O–W)
	243	ν(W–O–W)
326	323	ν(W–OH_2)
348	343	δ(W–O)
369	370	ν(W–OH_2)
—	417	Water libration
430	—	
—	453	
	554	
602	601	
618	617	
633	633	ν(W–O)
715	717	ν(W–O)
730	—	ν(W–O)
756	753	ν(O–W–O)
787	—	
	806	
816	—	ν(O–W–O)
	869	ν(O–W–O)
	926	
	961	ν(W=O)
970		ν(W=O)
	1012	
1039	1038	
	1093	
	1130	
	1184	
	1272	OH in plane bend
	1343	OH in plane bend
1377	—	OH-bend
1413	1408	Deformation OH
	1436	
	1481	C=C–C aromatic ring stretching due to PEG
1540		
1600		Deformation OH
1621	1621	Deformation OH
1805	1804	Aromatic combination bands
1828	1828	Aromatic combination bands
1947	1946	Aromatic combination bands
	2660	
2848		ν(C–H)
	2863	ν(C–H) due to PEG
2871		ν(C–H)
2918		ν(C–H)
	2928	ν(C–H)
2955	2958	ν(C–H)
3234	3234	ν(O–H)
3343	3343	ν(O–H)
3545	3545	ν(O–H) due to $WO_3 \cdot 2H_2O$
3560		ν(O–H)

326 cm^{-1}, and 234 cm^{-1}, which can be assigned to δ(W–O), ν(W–OH_2) and ν(W–O–W) vibrations, respectively.[59,67–69] The band at 369 cm^{-1} is attributed to the vibrational modes of water molecules.[67,69] The IR bands, located in the very low-frequency region (below 200 cm^{-1}) can be ascribed to lattice modes of WO_3 and its hydrates.[67] In particular, more intense ones are located at 182, 145, 120, and 105 cm^{-1}. The dominant broad band at 633 cm^{-1}, as well as the shoulders at 714 and 730 cm^{-1}, can be ascribed to the ν(W–O) vibrational modes.[67,69] The two shoulders identified by 2nd derivative analysis[50,70] are located around 816 and 970 cm^{-1}, and indexed as ν(O–W–O) and ν(W=O), respectively.[68] Furthermore, the ATR-IR spectrum of the sample WO_3_P_1 shows two IR bands at 1621 and 1600 cm^{-1} corresponding to the bending mode of H_2O molecules, which can be attributed to the water content in the sample.[71,72]

The ATR-IR spectrum of the WO_3_P_2 sample in the far-IR region shows main characteristic bands at 343 cm^{-1} (δ(W–O)), 323 cm^{-1} (ν(W–OH_2)), and 243 cm^{-1} (ν(W–O–W)).[59,67–69] The band at 370 cm^{-1} corresponds to the vibration modes of water molecules.[67,69] In the low-frequency region, main absorption bands due to WO_3 lattice modes and its hydrates are located at 178, 148, 120, and 105 cm^{-1}.[67] The intense broad band at 633 cm^{-1} and the evident shoulder at 718 cm^{-1} correspond to the ν(W–O) vibrational modes.[67,69] Two shoulders located around 753 and 869 cm^{-1} are indexed as ν(O–W–O) vibrations and can be ascribed to the bridging vibration of the corner-sharing WO_6 octahedron in the WO_3 crystal.[68,73] The weak bands in the spectral regions of 1450–1510 cm^{-1}, 1310–1410 cm^{-1}, and 1260–1350 cm^{-1} are associated with C=C–C aromatic ring stretching, O–H bend, and O–H in plane bend (observed in phenol), respectively. In particular, the bands located at 1481, 1343, and 1272 cm^{-1} can be attributed to the PEG 200.[74,75] The ATR-IR spectrum of WO_3_P_2 structure also shows an IR band at 1621 cm^{-1} due to the water content in the sample.

Considering Fig. 1(c), slight differences between WO_3_P_1 and WO_3_P_2 spectra can be recognized in the 600–1000 cm^{-1} spectral range. It is well established that all WO_3 polymorphs have vibrational spectra that differ from each other. However, most of the works in the literature do not describe the low-frequency range of 200–500 cm^{-1}.[69,72,76] Meanwhile, Fig. 1(c) clearly shows that the most significant differences between

WO_3_P_1 and WO_3_P_2 materials are observed in the low-frequency range (50–500 cm^{-1}). Here, both samples show absorption bands at 57, 72, 105, 120, 138, 145, 194, 323, and 370 cm^{-1}. Moreover, some significant differences in peak positions are observed between the WO_3_P_1 and WO_3_P_2 samples. The band located at 87 cm^{-1} (lattice mode) in the spectrum of WO_3_P_1 shifts to a higher frequency (92 cm^{-1}) in the spectrum of WO_3_P_2, while the peak at 182 cm^{-1} shifts to a lower frequency (178 cm^{-1}) in the spectrum of WO_3_P_2. The absorption band at 234 cm^{-1} in the spectrum of WO_3_P_1 (due to ν(W–O–W) vibration) shifts to a higher frequency (243 cm^{-1}) in that of WO_3_P_2. Finally, the absorption due to the W–O bending located at 348 cm^{-1} in the spectrum of WO_3_P_1 sample shifts to 343 cm^{-1} in that of WO_3_P_2. Furthermore, between the spectra of the materials, strong differences are evident in the mid-IR region, which can be attributed to the application of PEG 200 as a surfactant.[74,75]

The H_2O bending mode signal located at 1621 and 1600 cm^{-1} is more intense in the spectrum of WO_3_P_1 compared to that of WO_3_P_2, revealing a major water content in the sample prepared without using PEG. Besides, both samples exhibit vibrational bands above 3000 cm^{-1} due to the CH stretching of the benzyl alcohol solvent.

Fig. 2(a) and (b) show the surface morphologies of WO_3_P_1 and WO_3_P_2 materials obtained by FESEM. As can be seen, the structures consist of nanoparticles. It is worth noting that metal chloride, such as WCl_6, exhibits a strong polarization effect, and its high valence metal ions can be easily attacked by

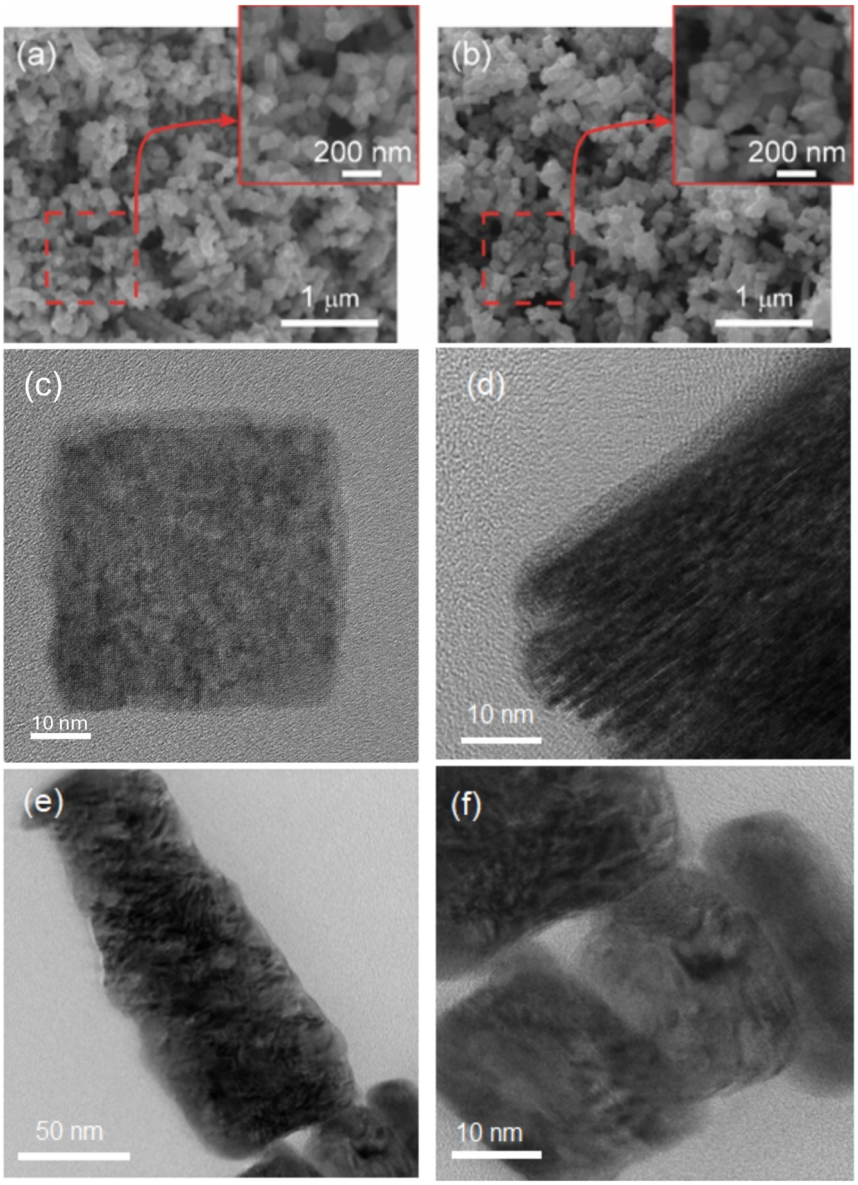

Fig. 2 (a) and (b) FESEM images of WO_3 nanostructures: (a) the morphology of WO_3_P_1 material and (b) the morphology of WO_3_P_2 material. (c) and (d) HRTEM images of a square nanoparticle WO_3_P_1: (c) WO_3 nanoparticle showing a very thin layer of amorphous material, and (d) another HRTEM image showing that the entire nanoparticle structure appears to be composed of a large number of very small nanorods. (e) and (f) HRTEM images of WO_3_P_2 nanoparticles.

a nucleophilic agent, resulting in high reactivity. Therefore, controlling the precipitation of WO_3 in a protic solvent is difficult.[77,78] The obtained morphological observations indicate that benzyl alcohol is a very suitable solvent to control the reaction rate of WCl_6 and the formation of particles. Benzyl alcohol can act as a solvation medium, oxygen supplier, and capping agent.[79–81] During our experimental process, the reaction of WCl_6 with benzyl alcohol leads to a color change from yellow to orange, light blue, and dark blue, which may indicate the formation of different charge transfer complexes by ligand exchange on tungsten atoms.[82,83] The color change to dark blue illustrates the partial reduction of W^{VI}.[82] Furthermore, the formation of WO_3 particles without agglomeration can be attributed to the stability of the carbocation intermediate formed during the reaction due to the direct bonding of the benzene ring with the α-carbon.[78]

Fig. 2(c) and (d) report high-resolution TEM (HRTEM) images of WO_3_P_1. In this case, the WO_3 nanoparticles are mainly square/rectangular and are surrounded by a very thin layer of amorphous material (about 3 nm). According to the results reported below (X-ray distribution of the elements, Fig. 3), this layer may be due to some residual ethanol used to cast the material on the TEM grid. In addition, as shown in Fig. 2(d), the entire nanoparticle consists of a large number of very thin nanorods (thickness: 1–2 nanometers), approximately aligned along one axis. Instead, the presence of PEG (sample WO_3_P_2), as shown in Fig. 2(e) and (f), increases the degree of disorder of the overall structure. This type of nanoparticle generally appears larger, thicker, and more irregular in shape, while the small nanorods described in Fig. 2(c) and (d) seem to disappear. The particle size distribution of WO_3_P_1 is shown in Fig. S1(a),† where it can be seen that most of the distribution is concentrated around 50 and 100 nm, with an average value of 93.86 ± 57.89 nm. From the size distribution shown in Fig. S1(b),† it is clear that the presence of PEG (WO_3_P_2 sample) leads to an increase in the size of WO_3 nanoaggregates, the average value of which is 120.45 ± 75.17 nm. The Gaussian particle size distribution for both materials is reported in Fig. S2.†

Fig. 3 shows the distribution of W, C, and O elements by EDX mapping for a WO_3_P_1 nanoparticle. The distribution of elements is quite homogeneous, and based on observations of intensity changes, the ratio of W and O is stable, while the presence of C is mainly due to the influence of the carbon-based membrane of the grid, although the presence of a slight

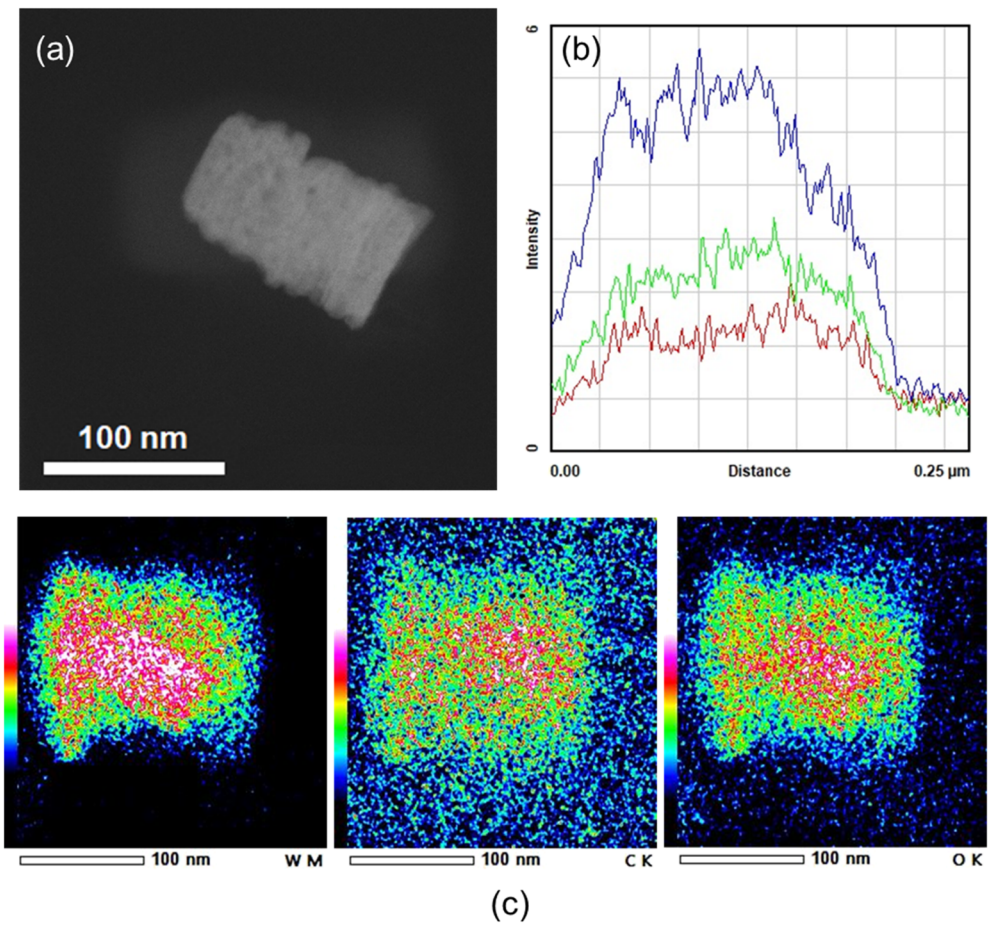

Fig. 3 EDX mapping of W, C, and O elements for a WO_3_P_1 nanoparticle: (a) STEM image of a WO_3 nanoparticle, (b) X-ray intensity profile of a single WO_3 nanoparticle (W – blue line, O – green line, C – red line), and (c) X-ray distribution map of the nanoparticle reported in (a) for C, O, and W.

increase in its intensity can be associated with some ethanol residues.

The X-ray intensity line profile in Fig. 4(b) indicates that the carbon and oxygen contents of WO_3_P_2 nanoparticles are higher than those of WO_3_P_1. An increased amount of carbon is also shown on the distribution map (Fig. 4(c)), where the presence of this chemical element is in the same area of the nanoparticle but also just outside the single particle, probably due to an excess of PEG.

Fig. S3(a)† shows the electron diffraction pattern of nanostructured WO_3_P_1, which shows a polycrystalline structure in which the different domains of the crystal have the same orientation on the main axis, but also small variations that transform the single diffraction spot into a short line. The SAED interpretation is consistent with the XRD signature corresponding to a monoclinic WO_3 structure oriented along the [100] zone axis, although the resulting *d*-spacings are higher than the expected values for monoclinic WO_3.[84] Table S1† shows the *d*-spacing of spots with higher intensity. In addition, the plane (002) can also be observed in the HRTEM image (Fig. S3(b)†).

In the case of the WO_3_P_2 material synthesized using PEG, the electron diffraction results at zero tilt are quite chaotic. They show weak signals indicating the presence of a polycrystal, as well as some intense spots that can be interpreted as (002) family lines (3.99 Å) for both orthorhombic and monoclinic structures, although they deviate slightly from the expected value (3.87 Å) (Fig. S4(a)†), probably due to the presence of PEG in the main crystalline structure. This interpretation is supported by the HRTEM image in Fig. S4(b),† where the calculated *d*-spacing is 4.02 Å, corresponding to the (002) line. These distances are suitable for both orthorhombic and monoclinic structures.

The XPS analyses indicate that the surface of both oxide films is composed of almost stoichiometric WO_3 (atomic ratio of about 2.8–3.0) with relatively low surface contamination by adventitious carbon and hydroxyl groups (Tables S2 and S3†). Therefore, for the compositional comparison of both samples, the film surface was cleaned by low-energy (1 keV) Ar^+ ion sputtering for a short time (60 s), removing about 0.6 nm of the film. After this cleaning, the surface contamination was removed, and the films were composed of three W species: WO_3, WO_2, and metallic W(0). The spectra of W 4f acquired for WO_3_P_1 and WO_3_P_2 samples after surface cleaning are presented in Fig. 5(a) and (b). After the application of the peak

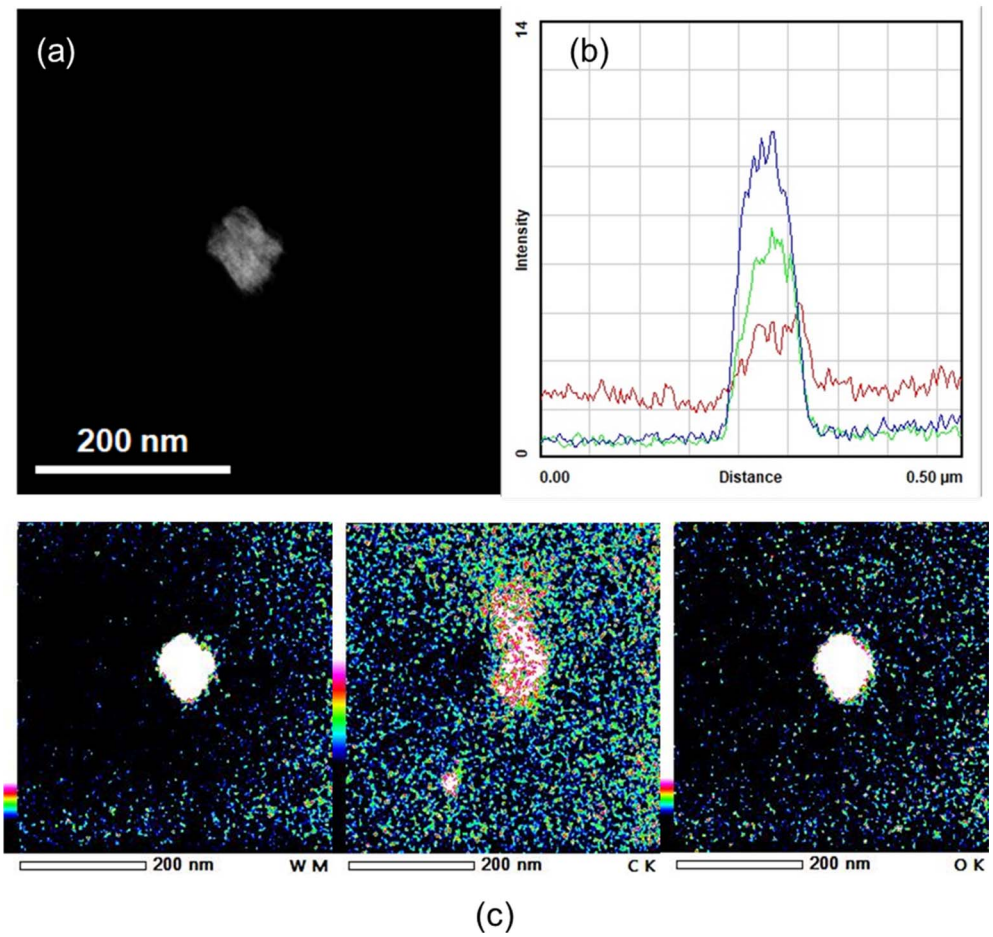

Fig. 4 EDX mapping of W, C, and O elements for a WO_3_P_2 nanoparticle: (a) STEM image of a WO_3 nanoparticle, (b) X-ray intensity profile of a single WO_3 nanoparticle (W – blue line, O – green line, C – red line), and (c) X-ray distribution map of the nanoparticle reported in (a) for C, O, and W.

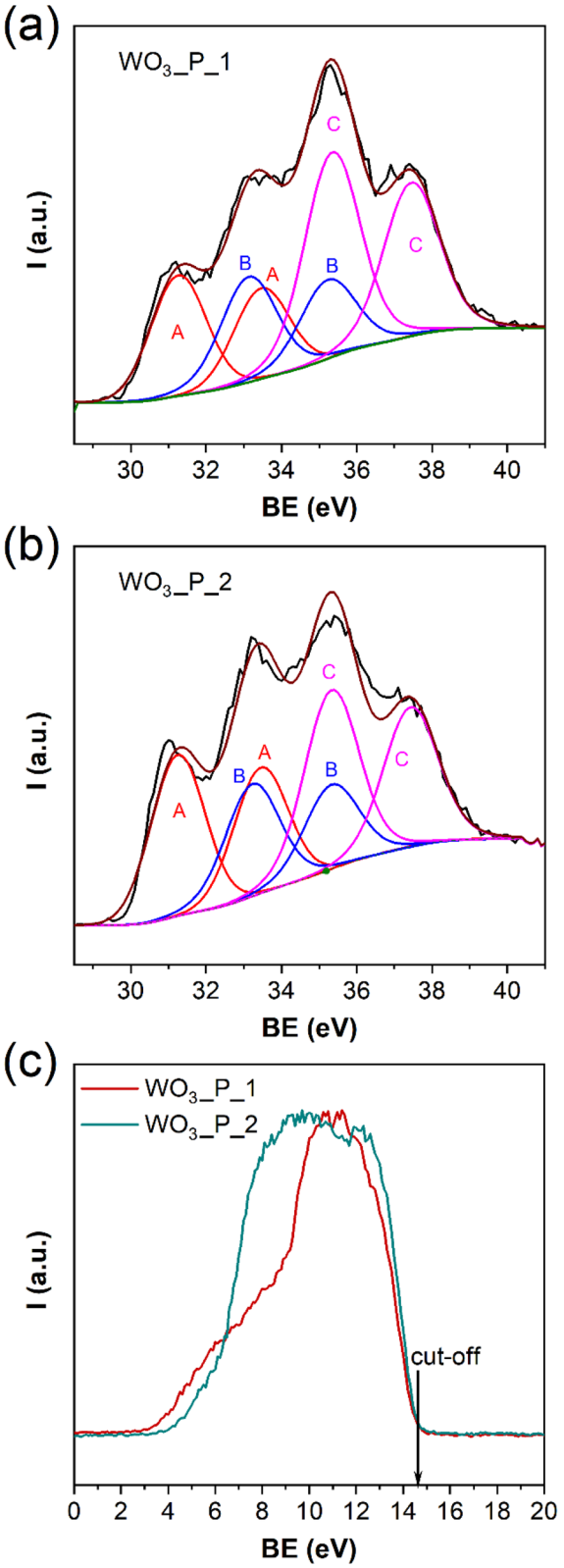

Fig. 5 W 4f photoemission spectra acquired for the (a) WO_3_P_1 and (b) WO_3_P_2 materials after surface cleaning by ion sputtering. Three spin–orbit doublets of W species revealed by peak fitting are marked as A, B, and C for W^0, W^{2+}, and W^{3+}, respectively. (c) He I valence band spectra acquired for the WO_3_P_1 and WO_3_P_2 materials.

fitting routine was revealed the presence of three W species with W $4f_{7/2}$ peaks at BE = 31.6 eV (A), 33.6 eV (B), and 35.7 eV (C), attributed to the species of W^0, W^{2+}, and W^{3+}, respectively. As follows from this comparison, the content of less coordinated W species (W^0 and W^{2+}) is noticeably higher in the WO_3_P_2 sample, where it is about 0.9 and 0.6 of stoichiometric W^{3+}, while in the WO_3_P_1 sample, it was only about 0.6 and 0.5, respectively. The UPS spectra of the valence band acquired for the WO_3_P_1 and WO_3_P_2 using a He I (21.2 eV) source are shown in Fig. 5(c). The obtained results indicate that there is no noticeable change in the valence band maxima (VBM).

3.2 Gas sensing results

Fig. 6(a) shows the response of WO_3_P_1 and WO_3_P_2 sensors to 10 ppm of acetone as a function of their operating temperature at 40% relative humidity (RH) in the test chamber. The response values of materials are listed in Table S4.† As can be seen, WO_3_P_1 is almost not sensitive to acetone (response value: 0.01) at 200 °C. The structure exhibits a good response (response value: 3) at 250 °C, which slightly enhances with an increase in the operating temperature to 300 °C (response value: 3.1). From 300 to 400 °C, the response curve has a larger slope and the response of the material reaches a maximum value (8.7) at 400 °C. A similar sensing behavior is observed for the WO_3_P_2 structure when the operating temperature is increased from 200 to 300 °C and then from 300 to 400 °C. However, in the temperature range of 300–400 °C, a significantly better enhancement of the response of WO_3_P_2 is observed (the response value increases from 9 to 62) compared to WO_3_P_1. Thus, the response of WO_3_P_2 nanomaterial to acetone is remarkably higher than that of WO_3_P_1.

Fig. 6(b) shows the dynamic response of the two materials to different concentrations of acetone at their optimum operating temperature. The baseline conductance of the sensors stabilizes in the air when the environmental oxygen is adsorbed on their surface. The capture of electrons by chemisorbed oxygen species is accompanied by the formation of an upward band bending at the surface of the semiconductor.[11] Then, the conductance values of structures enhance when exposed to acetone. This behavior is typical for n-type semiconductor materials due to the adsorption of reducing gaseous or volatile organic compounds on their surface.[85–88] In this case, the acetone molecules interact with adsorbed oxygen species on the surface of the structure, which leads to the trapped charge carriers being returned to the conduction band (eqn (1)).[42]

$$CH_3COCH_3(gas) + 8O^-(chemisorbed) \rightarrow 3CO_2 + H_2O + 8e^- \quad (1)$$

Afterward, the acetone flow is turned off, and the gas chamber is purified with a synthetic air flow. Herein, the recovery of the conductance of each sensor to its initial value in the air confirms the reversible sensing features of the materials. Furthermore, the response curves of both sensors as a function of acetone concentration (Fig. S5(a)†) confirm the superior functionality of WO_3_P_2 compared to WO_3_P_1 even at relatively low operating temperatures. Moreover, the WO_3_P_2

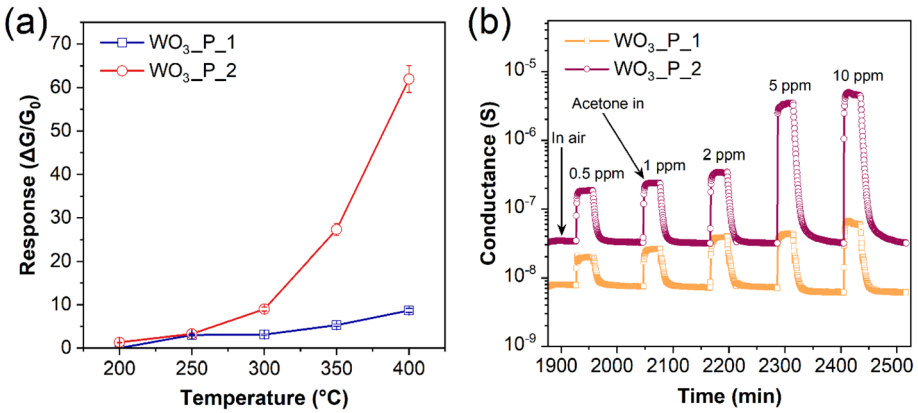

Fig. 6 (a) Response *vs.* temperature dependence of WO_3_P_1 and WO_3_P_2 sensors toward 10 ppm of acetone (RH, 40%). (b) Dynamic response of WO_3_P_1 and WO_3_P_2 toward different concentrations of acetone at a RH of 40%.

material exhibits an excellent response to very low concentrations (200 ppb) of acetone (Fig. S5(a) and Table S5†).

As we can see in Fig. 6(b) and S5(c),† the conductance of WO_3_P_2 increases when PEG is used as a surfactant. TEM studies of the sample prepared using PEG as a surfactant (WO_3_P_2) indicate that the nanoparticles are surrounded by a very thin layer of amorphous material. Besides, ATR-IR analyses demonstrate that several bands (*e.g.*, located at 1481, 1343, and 1272 cm^{-1}) can be attributed to residual PEG in the WO_3 matrix. Since PEG is a conductive material, the higher conductance of WO_3_P_2 compared to WO_3_P_1 is consistent with the results obtained from TEM and ATR-IR studies. Furthermore, the second slope of the Arrhenius plot for the WO_3_P_2 sample (0.19 eV, Fig. S5(b)†) correlates with the slope inherent in the pure PEG material (0.2 eV).[89] Based on the abovementioned facts, it cannot be excluded that PEG can influence the sorption processes, thereby increasing the sensitivity of the WO_3_P_2 material.

However, what is much more important is that the PEG surfactant displaces the water content of the material. Chacón *et al.* reported that when synthesizing WO_3 with low water concentration in the feed solution, the orthorhombic crystal structure is favored, while at higher water content, the monoclinic phase predominates.[90] This conclusion is fully consistent with our observations. Indeed, the XRD and Raman studies (Fig. 1(a) and (b)) indicate the presence of mixed orthorhombic and monoclinic phases in the WO_3_P_2 sample, while in the WO_3_P_1, only the monoclinic phase is detected.

Thus, suppressing hydrates and forming monoclinic/orthorhombic n–n junction in the WO_3 polymorph leads to a drastic increase in its sensitivity to acetone. At relatively low working temperatures (≤250 °C), acetone molecules are adsorbed on the WO_3 surface through the oxygen atoms of the carbonyl group attached to under-coordinated W cations on the surface.[91] Inhibition of hydrate formation by using PEG as a surfactant should increase the density of active adsorption sites on the material surface. Indeed, XPS analysis shows that the concentration of uncoordinated W atoms increased in WO_3_P_2 compared to WO_3_P_1 (Tables S2 and S3†). This could be the reason for the improved sensitivity of the WO_3_P_2 sample in the relatively low operating temperature range.

The formation of the monoclinic/orthorhombic junctions and their effect on the sensitivity of the material require more careful analysis. Our DFT calculations (Fig. 7) show that the monoclinic structure has a slightly larger indirect bandgap than the orthorhombic phase (2.57 eV *vs.* 2.51 eV, respectively). Although our theoretical simulations carried out with PBE0 functional slightly underestimate the experimental values determined for the monoclinic (2.62–2.7 eV)[92,93] and orthorhombic (2.58 eV)[94] phases of the WO_3 polymorph, the predicted trend remains the same.

Based on the Mott–Schottky plot, Kang *et al.* found that the conduction band minimum (CBM) of hexagonal h-WO_3 is located at about 0.1 eV higher than the CBM of the monoclinic γ-WO_3.[93] On the other hand, Y. Li *et al.* determined a downshift of 0.13 eV between the CBM of hexagonal h-WO_3 and orthorhombic β-WO_3 phases.[95] Our UPS investigations show that the VBM of nanomaterials WO_3_P_2 and WO_3_P_1 are located approximately at the same level (Fig. 5(c)).

Given our theoretical and experimental results in this work, we can deduce that the CBM of orthorhombic β-WO_3 is slightly lower (0.03–0.06 eV) than the CBM of monoclinic γ-WO_3 structure. Therefore, the electron transfer from the γ-WO_3 to the β-WO_3 counterpart leads to a further increase in the surface acidity of WO_3_P_2, where the monoclinic phase still dominates. The increased acidity of the WO_3_P_2 sample significantly facilitates the adsorption of acetone, which has weakly basic properties.

TEM characterization of the samples (Fig. 4(b)) demonstrates that the WO_3_P_2 sensor has a much higher oxygen content than the WO_3_P_1. According to eqn (1), the presence of oxygen is a necessary condition for the catalytic oxidation of acetone at elevated temperatures. Eventually, the increased oxygen content in the disordered WO_3_P_2 sensor can explain its significant sensitivity to acetone in the high-temperature operating range.

We also investigated the effect of RH on the electrical and sensing properties of synthesized materials by gradually increasing its concentration in the test chamber to 95%

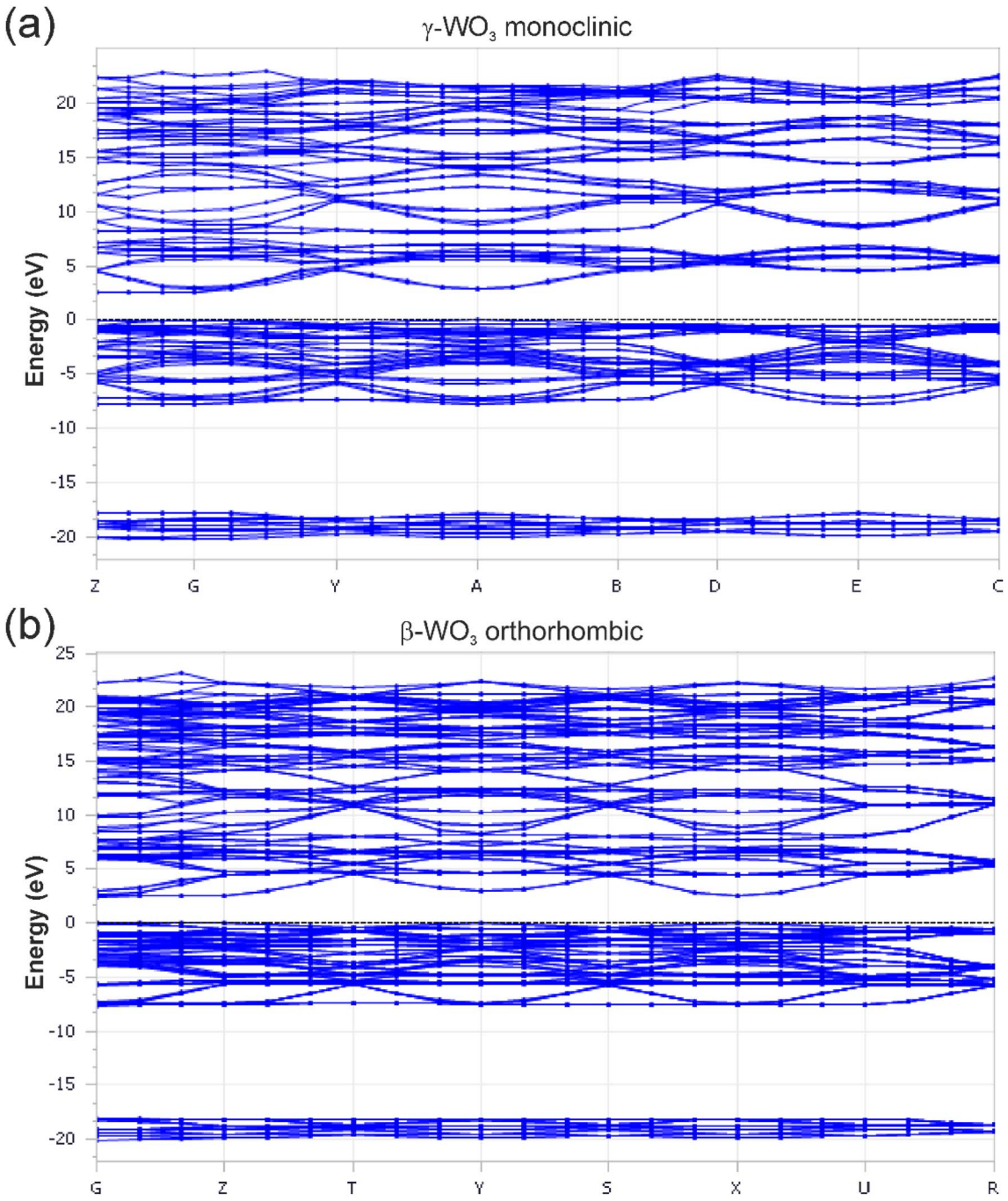

Fig. 7 Calculations of the electronic band structure of the monoclinic γ-WO_3 (a) and orthorhombic phases of β-WO_3 (b). Zero energy corresponds to the top of the valence band.

(Fig. S5(c)† and 8(a)). The obtained results indicate that there are no significant changes in the conductance and response of the WO_3_P_1 and WO_3_P_2 sensors due to the increase in the RH level in the chamber, even at a low concentration of acetone (200 ppb). Fig. 8(b) shows the response of WO_3_P_1 and WO_3_P_2 toward other gaseous compounds. Here, the high selectivity of both materials is evident. In particular, WO_3_P_2 exhibits excellent sensing performance to acetone. Furthermore, we measured the dynamic response of the polymorphic WO_3_P_2 sensing material to different concentrations of acetone at 400 °C over two consecutive exposure cycles. The structure conductance returns to its baseline value in air after the injection of each concentration of acetone into the test chamber and its subsequent purification during both test cycles (Fig. S6†), demonstrating the reliability of the obtained results. We also compared its acetone sensing parameters with those of other semiconductor gas sensors based on pure and composite structures (Table S6†). As can be seen, the nanostructuration of WO_3 and appropriate modification of its crystalline structure have a crucial effect on its functionality.

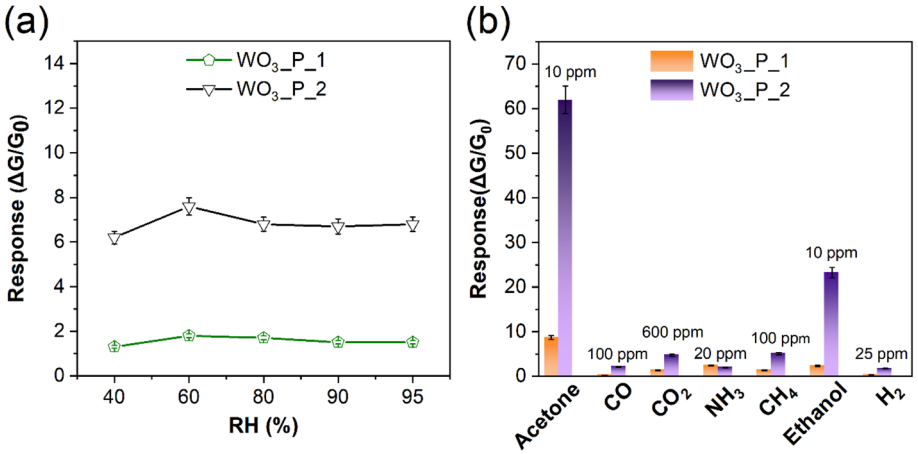

Fig. 8 (a) Response values of WO_3_P_1 and WO_3_P_2 sensors to 200 ppm of acetone at different concentrations of RH (40–95%) in the test chamber. The operating temperature of the sensors is 400 °C. (b) Sensing response of WO_3_P_1 and WO_3_P_2 toward different gaseous and volatile organic compounds at their optimum operating temperature (400 °C).

4. Conclusions

In summary, we synthesized and studied the monoclinic/orthorhombic WO_3 polymorph nanomaterials for their application in chemical gas sensing devices. The precipitation method is an effective approach to obtain nanostructured WO_3, where benzyl alcohol is crucial for controlling the reaction rate of the WCl_6 precursor and the precipitation of material. Thus, it can be used to prepare WO_3 nanoparticles. The addition of PEG in the synthesis process increases structural disorder and suppresses hydrate formation in the resulting WO_3 nanomaterial. Furthermore, PEG surfactant affects the oxygen content in WO_3 and promotes partial crystallization of the material into the orthorhombic structure.

Without the addition of PEG, the water content of WO_3 annealed at 450 °C is higher, and the material tends to crystallize into the monoclinic phase. In contrast, the material synthesized using PEG and annealed at 450 °C still predominantly exhibits the monoclinic phase, but a contribution from orthorhombic phases can also be observed. Our experimental and theoretical results demonstrate that hydrate reduction and the formation of monoclinic/orthorhombic n–n junctions in the WO_3 polymorph are critical factors in enhancing its interaction with acetone. The reduction of hydrates increases the density of active adsorption sites on the surface of the material, which is favorable for the adsorption of acetone. Moreover, the electronic band structure in the monoclinic/orthorhombic polymorph results in electron transfer from the γ-WO_3 to the β-WO_3, increasing the acidity of WO_3 and enhancing its interaction with acetone. Furthermore, the higher oxygen content of the material prepared using PEG facilitates the catalytic oxidation of acetone at elevated temperatures and thus improves its sensing response at relatively high operating temperatures.

The high sensing response and selectivity of the WO_3 sample prepared with the addition of PEG, as well as its stable functionality at different humidity levels, indicate that the polymorphism in the WO_3 nanomaterial, considering the appropriate modification of crystalline phases in the structure, may lead to a wider use of WO_3 in chemical gas sensing and photocatalytic processes.

Data availability

All data supporting the findings of this study are available within the article and its ESI.†

Author contributions

Hakimeh Pakdel: conceptualization, formal analysis, investigation, methodology, validation, visualization, writing – original draft; Vardan Galstyan: conceptualization, data curation, formal analysis, funding acquisition, investigation, methodology, project administration, supervision, validation, visualization, writing – original draft, writing – review & editing; Viacheslav Golovanov: data curation, formal analysis, funding acquisition, investigation, methodology, software, validation, visualization, writing – original draft, writing – review & editing; Annalisa D'Arco: formal analysis, investigation, methodology, validation, visualization, writing – original draft, writing – review & editing; Tiziana Mancini: formal analysis, investigation, methodology, validation, visualization, writing – original draft; Francesco Mura: formal analysis, investigation, methodology, validation, writing – original draft; Marco Rossi: funding acquisition, methodology, resources, writing – review & editing; Stefano Lupi: funding acquisition, methodology, resources, writing – review & editing; Alessio Mezzi: formal analysis, investigation, methodology, validation, visualization, writing – original draft; Saulius Kaciulis: funding acquisition, investigation, methodology, resources, writing – original draft, writing – review & editing; Elisabetta Comini: funding acquisition, methodology, resources, project administration, writing – review & editing.

Conflicts of interest

There are no conflicts to declare.

Acknowledgements

Viacheslav Golovanov is grateful to the Research Council of Finland (grant no. 367543) and the MSCA4Ukraine grant (no. 1233501), which is funded by the European Union. Views and opinions expressed are, however, those of the author(s) only and do not necessarily reflect those of the European Union. Neither the European Union nor the MSCA4Ukraine Consortium as a whole nor any individual member institutions of the MSCA4Ukraine Consortium can be held responsible for them. Computational resources were provided by the CSC-IT Centre for Science, Espoo, Finland.

References

1 D. Huang, Y. Wang, X. Wang, H. Li, X. Tan, Y. Chen, W. Wang, Q. Cheng, M. Yi, G. Han and G. Liu, *Chem. Eng. J.*, 2022, **444**, 136526.
2 T. Zhou and T. Zhang, *Small Methods*, 2021, **5**, 2100515.
3 M. Ye, X. Hong, F. Zhang and X. Liu, *J. Mater. Chem. A*, 2016, **4**, 6755–6771.
4 Z. Wang, Q. Wang, Y. Han, Y. Ma, H. Zhao, A. Nowak and J. Li, *Energy Storage Mater.*, 2021, **39**, 45–53.
5 V. Galstyan, J. M. Macak and T. Djenizian, *Appl. Mater. Today*, 2022, **29**, 101613.
6 M. Zhou, Y. Li and G. Xu, *TrAC, Trends Anal. Chem.*, 2024, **174**, 117679.
7 R. Jana, S. Hajra, P. M. Rajaitha, K. Mistewicz and H. J. Kim, *J. Environ. Chem. Eng.*, 2022, **10**, 108543.
8 J. Bai, Y. Shen, S. Zhao, A. Li, Z. Kang, B. Cui, D. Wei, Z. Yuan and F. Meng, *Adv. Mater. Technol.*, 2023, **8**, 2201671.
9 T. K. Stewart, I. E. Carotti, Y. M. Qureshi and J. A. Covington, *TrAC, Trends Anal. Chem.*, 2024, **177**, 117792.
10 S. Mahajan and S. Jagtap, *Appl. Mater. Today*, 2020, **18**, 100483.
11 V. Galstyan, *Anal. Chim. Acta*, 2021, **1152**, 238192.
12 S. Cao, Y. Xu, Z. Yu, P. Zhang, X. Xu, N. Sui, T. Zhou and T. Zhang, *Small*, 2022, **18**, 2203715.
13 K. Wu, M. Debliquy and C. Zhang, *Compr. Rev. Food Sci. Food Saf.*, 2023, **22**, 913–945.
14 Z. Shi, L. Lin, R. Chen and L. Yan, *Mater. Today Commun.*, 2021, **28**, 102699.
15 M. Valt, M. Caporali, B. Fabbri, A. Gaiardo, S. Krik, E. Iacob, L. Vanzetti, C. Malagù, M. Banchelli, C. D'Andrea, M. Serrano-Ruiz, M. Vanni, M. Peruzzini and V. Guidi, *ACS Appl. Mater. Interfaces*, 2021, **13**, 44711–44722.
16 A. Fioravanti and M. C. Carotta, *Appl. Sci.*, 2020, **10**, 1741.
17 X. Li, T. Tan, W. Ji, W. Zhou, Y. Bao, X. Xia, Z. Zeng and Y. Gao, *Energy Environ. Mater.*, 2023, **7**, e12624.
18 M. Ikram, L. Liu, Y. Liu, L. Ma, H. Lv, M. Ullah, L. He, H. Wu, R. Wang and K. Shi, *J. Mater. Chem. A*, 2019, **7**, 14602–14612.
19 V. Galstyan, A. Ponzoni, I. Kholmanov, M. M. Natile, E. Comini, S. Nematov and G. Sberveglieri, *ACS Sens.*, 2019, **4**, 2094–2100.
20 Y. He and M. Jiao, *Chemosensors*, 2024, **12**, 55.
21 F. Yang, Y. Hu, Q. Hu, S. Steiner, T. Frömling, L. Li, P. Wu, E. Pradal-Velázquez and D. C. Sinclair, *J. Mater. Chem. A*, 2022, **10**, 891–901.
22 S. Akrami, M. Watanabe, T. H. Ling, T. Ishihara, M. Arita, M. Fuji and K. Edalati, *Appl. Catal., B*, 2021, **298**, 120566.
23 K. Bourikas, C. Kordulis and A. Lycourghiotis, *Chem. Rev.*, 2014, **114**, 9754–9823.
24 J. Ma, W. Xie, J. Li, H. Yang, L. Wu, Y. Zou and Y. Deng, *Small*, 2023, **19**, 2301011.
25 H. Y. Kim, H. Kong, J. H. Kim, W.-G. Yang, H. Lee, S. Ko, H. J. Lee, G. Piao, H. Park, W.-S. Chae and J. Yeo, *J. Mater. Chem. A*, 2023, **11**, 4598–4607.
26 X. Dai, Y. Tian, A. Meng, L. Wang, G. Li, J. Huang, X. Yu, S. Ding and Z. Li, *Energy Storage Mater.*, 2023, **57**, 125–135.
27 C. Zhang, X. Zheng, Y. Ning, Z. Li, Z. Wu, X. Feng, G. Li, Z. Huang and Z. Hu, *J. Energy Chem.*, 2023, **80**, 584–593.
28 C. V. Ramana, S. Utsunomiya, R. C. Ewing, C. M. Julien and U. Becker, *J. Phys. Chem. B*, 2006, **110**, 10430–10435.
29 F. Jafari and M. B. Gholivand, *Mater. Today Chem.*, 2023, **29**, 101432.
30 S. Jiang, B. Luo, K. Li, Y. Yin, Z. Zhang, T. Zhu and X. Li, *J. Cleaner Prod.*, 2023, **397**, 136621.
31 J. Besnardiere, B. Ma, A. Torres-Pardo, G. Wallez, H. Kabbour, J. M. González-Calbet, H. J. Von Bardeleben, B. Fleury, V. Buissette, C. Sanchez, T. Le Mercier, S. Cassaignon and D. Portehault, *Nat. Commun.*, 2019, **10**, 327.
32 Z. Wang, C. Zhu, Z. Ni, H. Hojo and H. Einaga, *ACS Catal.*, 2022, **12**, 14976–14989.
33 S. Li, J. Wang, Y. Xia, P. Li, Y. Wu, K. Yang, Y. Song, S. Jiang, T. Zhang and B. Li, *Chem. Eng. J.*, 2021, **417**, 129298.
34 T. Feng, Z. Cui, P. Guo, X. Wang, J. Li, X. Liu, W. Wang and Z. Li, *J. Colloid Interface Sci.*, 2023, **636**, 618–626.
35 B. Lei, W. Cui, P. Chen, L. Chen, J. Li and F. Dong, *ACS Catal.*, 2022, **12**, 9670–9678.
36 B. Li, Z. Wang, S. Zhao, C. Hu, L. Li, M. Liu, J. Zhu, T. Zhou, G. Zhang, J. Jiang and C. Zou, *Small Methods*, 2022, **6**, 2200931.
37 Y. Zhang, T. Wu, D. Liu, R. Xu, H. Ma, Q. Wei and Y. Zhang, *Biosens. Bioelectron.*, 2022, **213**, 114452.
38 L. Bai, S. Jia, Y. Gao, C. Li, X. Chen, S. Zhou, J. Han, F. Yang, X. Zhang and S. Lu, *Energy Environ. Mater.*, 2023, **6**, e12456.
39 M. A. Mahadik, I.-S. Hwang, W.-S. Chae, H. H. Lee, S. H. Choi, M. Cho and J. S. Jang, *Chemosphere*, 2023, **318**, 137973.
40 B.-R. Chen, W. Sun, D. A. Kitchaev, J. S. Mangum, V. Thampy, L. M. Garten, D. S. Ginley, B. P. Gorman, K. H. Stone, G. Ceder, M. F. Toney and L. T. Schelhas, *Nat. Commun.*, 2018, **9**, 2553.
41 P. Li, Z. Zhang, Z. Zhuang, J. Guo, Z. Fang, S. L. Fereja and W. Chen, *Anal. Chem.*, 2021, **93**, 7465–7472.
42 V. Galstyan, N. Poli, A. D'Arco, S. Macis, S. Lupi and E. Comini, *J. Mater. Chem. A*, 2020, **8**, 20373–20385.
43 K. Yuan, C.-Y. Wang, L.-Y. Zhu, Q. Cao, J.-H. Yang, X.-X. Li, W. Huang, Y.-Y. Wang, H.-L. Lu and D. W. Zhang, *ACS Appl. Mater. Interfaces*, 2020, **12**, 14095–14104.
44 I. M. Szilágyi, B. Fórizs, O. Rosseler, Á. Szegedi, P. Németh, P. Király, G. Tárkányi, B. Vajna, K. Varga-Josepovits,

K. László, A. L. Tóth, P. Baranyai and M. Leskelä, *J. Catal.*, 2012, **294**, 119–127.
45 X. Zhang, B. Dong, W. Liu, X. Zhou, M. Liu, X. Sun, J. Lv, L. Zhang, W. Xu, X. Bai, L. Xu, S. Mintova and H. Song, *Sens. Actuators, B*, 2020, **320**, 128405.
46 H. J. Choi, J.-H. Chung, J.-W. Yoon and J.-H. Lee, *Sens. Actuators, B*, 2021, **338**, 129823.
47 J. Zhang, H. Lu, H. Lu, G. Li, J. Gao, Z. Yang, Y. Tian, M. Zhang, C. Wang and Z. He, *J. Alloys Compd.*, 2019, **779**, 531–542.
48 J. K. Kim, K. Shin, S. M. Cho, T.-W. Lee and J. H. Park, *Energy Environ. Sci.*, 2011, **4**, 1465–1470.
49 C. Santato, M. Odziemkowski, M. Ulmann and J. Augustynski, *J. Am. Chem. Soc.*, 2001, **123**, 10639–10649.
50 F. Piccirilli, F. Tardani, A. D'Arco, G. Birarda, L. Vaccari, S. Sennato, S. Casciardi and S. Lupi, *Nanomaterials*, 2021, **11**, 1103.
51 V. Galstyan, E. Comini, C. Baratto, A. Ponzoni, M. Ferroni, N. Poli, E. Bontempi, M. Brisotto, G. Faglia and G. Sberveglieri, *Sens. Actuators, B*, 2015, **209**, 1091–1096.
52 V. Galstyan, A. Ponzoni, I. Kholmanov, M. M. Natile, E. Comini, S. Nematov and G. Sberveglieri, *ACS Sens.*, 2019, **4**, 2094–2100.
53 V. V. Golovanov, M. A. Maki-Jaskari and T. T. Rantala, *IEEE Sens. J.*, 2002, **2**, 416–421.
54 V. Milman, B. Winkler, J. White, C. Pickard, M. Payne, E. Akhmatskaya and R. Nobes, *Int. J. Quantum Chem.*, 2000, **77**, 895–910.
55 C. Adamo and V. Barone, *Chem. Phys. Lett.*, 1999, **314**, 152–157.
56 H. J. Monkhorst and J. D. Pack, *Phys. Rev. B*, 1976, **13**, 5188.
57 Y. Li, Z. Liu, X. Liang, J. Ya, T. Cui and Z. Liu, *Mater. Technol.*, 2014, **29**, 341–349.
58 C. Santato, M. Odziemkowski, M. Ulmann and J. Augustynski, *J. Am. Chem. Soc.*, 2001, **123**, 10639–10649.
59 M. Daniel, B. Desbat, J. Lassegues, B. Gerand and M. Figlarz, *J. Solid State Chem.*, 1987, **67**, 235–247.
60 U. O. Krašovec, A. Š. Vuk and B. Orel, *Electrochim. Acta*, 2001, **46**, 1921–1929.
61 E. Cazzanelli, C. Vinegoni, G. Mariotto, A. Kuzmin and J. Purans, *J. Solid State Chem.*, 1999, **143**, 24–32.
62 K. Thummavichai, N. Wang, F. Xu, G. Rance, Y. Xia and Y. Zhu, *R. Soc. Open Sci.*, 2018, **5**, 171932.
63 M. P. Thi and G. Velasco, *Solid State Ionics*, 1984, **14**, 217–220.
64 B. Pecquenard, H. Lecacheux, J. Livage and C. Julien, *J. Solid State Chem.*, 1998, **135**, 159–168.
65 G. Ramans, J. Gabrusenoks and A. Veispals, *Phys. Status Solidi A*, 1982, **74**, K41–K44.
66 R. F. Garcia-Sanchez, T. Ahmido, D. Casimir, S. Baliga and P. Misra, *J. Phys. Chem. A*, 2013, **117**, 13825–13831.
67 M. Gotić, M. Ivanda, S. Popović and S. Musić, *Mater. Sci. Eng., B*, 2000, 77, 193–201.
68 C. Balázsi, M. Farkas-Jahnke, I. Kotsis, L. Petrás and J. Pfeifer, *Solid State Ionics*, 2001, **141–142**, 411–416.
69 G. N. Kustova, Y. A. Chesalov, L. M. Plyasova, I. Y. Molina and A. I. Nizovskii, *Vib. Spectrosc.*, 2011, **55**, 235–240.
70 A. D'Arco, M. Di Fabrizio, T. Mancini, R. Mosetti, S. Macis, G. Tranfo, G. Della Ventura, A. Marcelli, M. Petrarca and S. Lupi, *Int. J. Mol. Sci.*, 2023, **24**, 9550.
71 S. M. Kanan and C. P. Tripp, *Curr. Opin. Solid State Mater. Sci.*, 2007, **11**, 19–27.
72 T. M. Bushkova, A. A. Egorova, A. V. Khoroshilov, O. S. Ivanova, A. D. Yapryntsev, A. E. Baranchikov and V. K. Ivanov, *Russ. J. Inorg. Chem.*, 2021, **66**, 496–501.
73 H. F. Pang, X. Xiang, Z. J. Li, Y. Q. Fu and X. T. Zu, *Phys. Status Solidi A*, 2012, **209**, 537–544.
74 Z. Varga, J. Mihály, S. Berényi and A. Bóta, *Eur. Polym. J.*, 2013, **49**, 2415–2421.
75 K. Shameli, M. B. Ahmad, S. D. Jazayeri, S. Sedaghat, P. Shabanzadeh, H. Jahangirian, M. Mahdavi and Y. Abdollahi, *Int. J. Mol. Sci.*, 2012, **13**, 6639–6650.
76 R. Hatel and M. Baitoul, *Mater. Chem. Phys.*, 2019, **225**, 169–173.
77 X.-L. Li, T.-J. Lou, X.-M. Sun and Y.-D. Li, *Inorg. Chem.*, 2004, **43**, 5442–5449.
78 M. Hu, J. Xu, J. Gao, S. Yang, J. S. P. Wong and R. K. Y. Li, *Dalton Trans.*, 2013, **42**, 9777–9784.
79 M. Niederberger, M. H. Bartl and G. D. Stucky, *Chem. Mater.*, 2002, **14**, 4364–4370.
80 D. Malwal and G. Packirisamy, *Synthesis of Inorganic Nanomaterials*, 2018, pp. 255–281.
81 M. Niederberger, N. Pinna, J. Polleux and M. Antonietti, *Angew. Chem.*, 2004, **116**, 2320–2323.
82 I. Olliges-Stadler, J. Stötzel, D. Koziej, M. D. Rossell, J.-D. Grunwaldt, M. Nachtegaal, R. Frahm and M. Niederberger, *Chem.–Eur. J.*, 2012, **18**, 2305–2312.
83 M. Niederberger, *Acc. Chem. Res.*, 2007, **40**, 793–800.
84 S. Tanisaki, *J. Phys. Soc. Jpn.*, 1960, **15**, 573–581.
85 V. Golovanov, V. Smyntyna, G. Mattogno, S. Kaciulis and V. Lantto, *Sens. Actuators, B*, 1995, **26**, 108–112.
86 R. Abdelghani, H. Shokry Hassan, I. Morsi and A. B. Kashyout, *Sens. Actuators, B*, 2019, **297**, 126668.
87 V. Golovanov, V. Golovanova and T. T. Rantala, *J. Phys. Chem. Solids*, 2016, **89**, 15–22.
88 G. Korotcenkov, V. Golovanov, V. Brinzari, A. Cornet, J. Morante and M. Ivanov, *J. Phys.: Conf. Ser.*, 2005, **15**, 256.
89 M. Murugendrappa, S. Khasim and M. Prasad, *Indian J. Eng. Mater. Sci.*, 2020, **7**, 456–458.
90 C. Chacón, M. Rodríguez-Pérez, G. Oskam and G. Rodríguez-Gattorno, *J. Mater. Sci.: Mater. Electron.*, 2015, **26**, 5526–5531.
91 S. Americo, E. Pargoletti, R. Soave, F. Cargnoni, M. I. Trioni, G. L. Chiarello, G. Cerrato and G. Cappelletti, *Electrochim. Acta*, 2021, **371**, 137611.
92 V. Guidi, M. Blo, M. Butturi, M. Carotta, S. Galliera, A. Giberti, C. Malagù, G. Martinelli, M. Piga and M. Sacerdoti, *Sens. Actuators, B*, 2004, **100**, 277–282.
93 M. Kang, J. Liang, F. Wang, X. Chen, Y. Lu and J. Zhang, *Mater. Res. Bull.*, 2020, **121**, 110614.
94 A. K. H. Bashir, R. Morad, A. C. Nwanya, M. Akbari, J. Sackey, K. Kaviyarasu, I. G. Madiba, F. I. Ezema and M. Maaza, *J. Nanopart. Res.*, 2021, **23**, 31.
95 Y. Li, Z. Tang, J. Zhang and Z. Zhang, *Appl. Catal., B*, 2017, **207**, 207–217.

